ELSEVIER

Journal of Alloys and Compounds 330–332 (2002) 34–40

Journal of ALLOYS AND COMPOUNDS

www.elsevier.com/locate/jallcom

On the accuracy of heat flux calorimetry in stable intermetallic–H_2(g) systems

P. Dantzer*, P. Millet

CNRS – UMR 8647, bât 415, Université Paris Sud, 91405 Orsay Cedex, France

Abstract

Heat flux calorimetry used for the determination of enthalpies of hydride formation falls into a non-routine class as shown by the conflicting data in the literature for seemingly identical systems. Problems can also appear with a non-appropriate use of the calorimeter as for example, if the hydrogen gas pressure is in the Knudsen regime. In that case, errors can arise from changes of the thermal transfer path within the cell. This and other problems associated with the determination of the enthalpies of hydride formation will be addressed in this paper. The analysis will be made on the ZrNi–H_2 system.

Keywords: Heat flux calorimetry; First order transition; Enthalpy; Heat transfer; Modeling; Intermetallic hydrides

1. Introduction

Since the first appearance of commercial heat flux (heat conduction) calorimeters in the 1960s, continuous improvements have been made [1–4]. At present, the units operating with powerful software allow data to be readily obtained, but the data are of doubtful validity, in some cases [7]. This is particularly true when the measurements are non-routine [5,6].

Calorimetry applied to the determination of enthalpy of phase transformation in intermetallic compounds–H_2 (IMC–H_2) systems falls into the non-routine class as shown by the conflicting data in the literature for seemingly identical systems. It is mainly due to the problems associated with the hydrogen gas-induced solid state transformation:

$$(b-a)^{-1}\mathrm{MH}_a + \frac{1}{2}\mathrm{H}_2(\mathrm{plat,g}) \rightarrow (b-a)^{-1}\mathrm{MH}_b, \qquad (1)$$

a, b represent the hydrogen contents at the phase boundaries, MH_a and MH_b the solid solution and the hydride compound, respectively, or two hydrides. In the two phase domain, the calorimeter measures the heat of transformation. The shape of the thermograms depends on the heat transfer conditions in the reactor which can be influenced by the irreversible character of the transformation and by the low thermal conductivity of the powdered material which can produce significant non-isothermal behaviour. A problem can also be generated if the hydrogen gas remains in the molecular regime (Knudsen regime). This problem is addressed in the paper where the thermodynamic characterisation of the important ZrNi–H_2 system has been made with a calorimeter coupled with a volumetric device. For ZrNi–H_2, a great interest is justified for isotope storage, separation technology [8,9], in closed-cycle cryocoolers [10]. Knowledge of accurate thermodynamic parameters is very important for any application.

The paper is organized as follows: after a brief overview on ZrNi–H_2 and a short description of the experimental set-up we present the heat measurements obtained across the domain of the Knudsen regime and the models developed to analyze the thermograms.

2. ZrNi–H_2 system

ZrNi was the first IMC investigated for its hydrogen absorption properties by Libowitz et al. [11] and later by Kost et al. [12]. Westlake et al. [13] determined two structures corresponding to a triclinic monohydride phase ZrNiH and an orthorhombic trihydride phase $ZrNiH_3$. Recent band structure calculations [14] have shown that in the ZrNiH phase, the preferred occupancy of the tetrahedral Zr_4 over the Zr_3Ni sites is associated with chemical effects rather than geometric factors such as hole size and H–H distances. Since the earlier reports, the most exten-

*Corresponding author.

E-mail address: pierre.dantzer@lemhe.u-psud.fr (P. Dantzer).

0925-8388/02/$ – see front matter
PII: S0925-8388(01)01650-4

sive thermodynamic studies of the system were carried out by Luo et al. [15]. Recently, the temperature dependence of the relative enthalpy of transformation for the β to γ formation of $ZrNiH_{3-\delta}$ was determined by Dantzer et al. [16].

3. Experimental

- Apparatus: a full description of the equipment (Fig. 1), details of the procedure and of the calibration of the calorimeter, and analysis of the uncertainties, are found in Ref. [1].
- Reactor: with regard to the thermopile, the reactor is an open system. Any heat transport modification through the gas phase is detected with fast response thermocouples which are mounted in the reactor. They act as a second thermal sensor measuring any modification of the thermal losses above the thermopile.
- Sample: two samples of ZrNi were used. Sample 1 intentionally contained traces of cerium oxide (<1%) making it brittle. Sample 2 is of very high purity. Microprobe analysis of the latter did not show any significant impurities but possible compositional inhomogeneities, traces of Zr_9Ni_{11}. XRD did not show the presence of other phases.

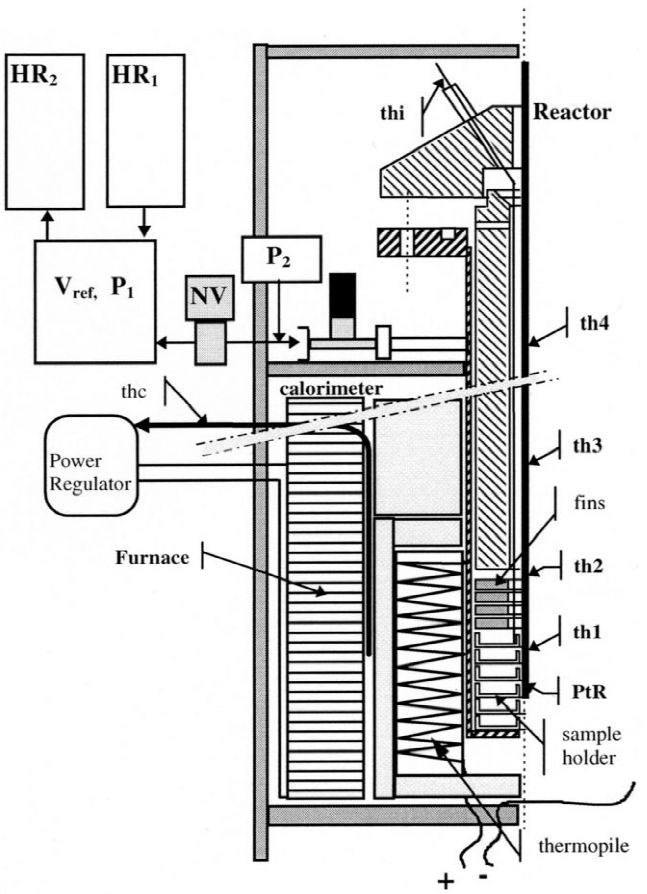

Fig. 1. Schematic drawing of the gas distribution coupled with the calorimeter. HR, hydride reservoir; NV, needle valve; thi, thermocouple i.

4. Heat measurements

Investigations have been carried out at 116.3, 126.6, 152.6 and 191.2°C for sample 1 and 210.6° and 226°C for sample 2.

4.1. Heat transfer in the low pressure range

The sample holder is in a loose contact with the inner wall of the reactor making the signal detected by the thermopile sensitive to the gas pressure because heat is transmitted through the wall both by the sample holder and the gas. During calibration, heat transfer through the gas remains in a steady state. Hydrogen loading must not modify the heat losses through the gas phase otherwise erroneous heat determinations will be obtained despite the accuracy of the calibration coefficient. In spite of the precautions taken, it is difficult to satisfy because the thermal conductivity of the gas, λ_{H_2}, depends on the pressure and the temperature [17]. In Fig. 2 the sharp variation in the 'S' shaped curve is observed when λ_{H_2} diminishes markedly below $P \approx 10$ kPa.

4.2. Results

Thermograms obtained in the two-phase region, corresponding to the formation of $ZrNiH_{3-\delta}$ are shown in Fig. 3. Fig. 4 shows the time-dependent temperature variations in the reactor for one representative experiment in the series. Thermograms in Fig. 3a clearly show an endothermal contribution which disappears at 152.9°C (Fig. 3b,

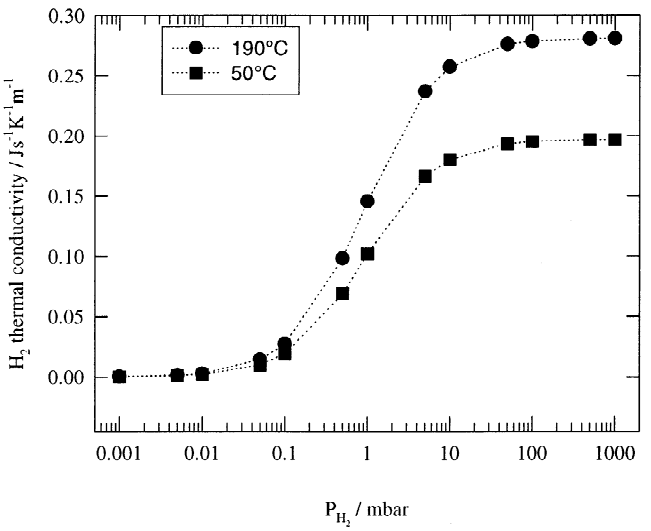

Fig. 2. Thermal conductivity of the hydrogen gas vs. *P*, 1 mbar = 10^2 Pa.

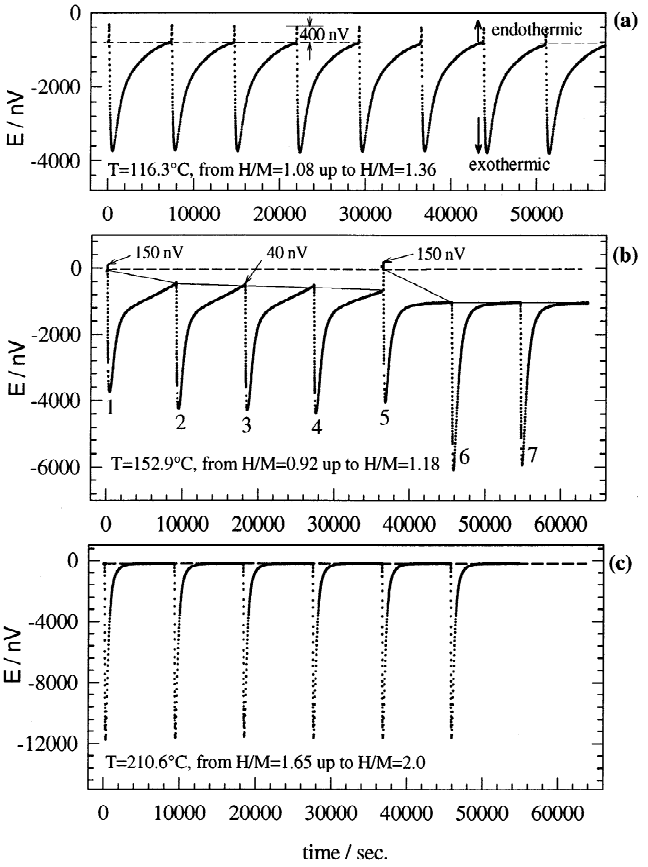

Fig. 3. The observed responses of the calorimeter for sequential additions of identical hydrogen doses.

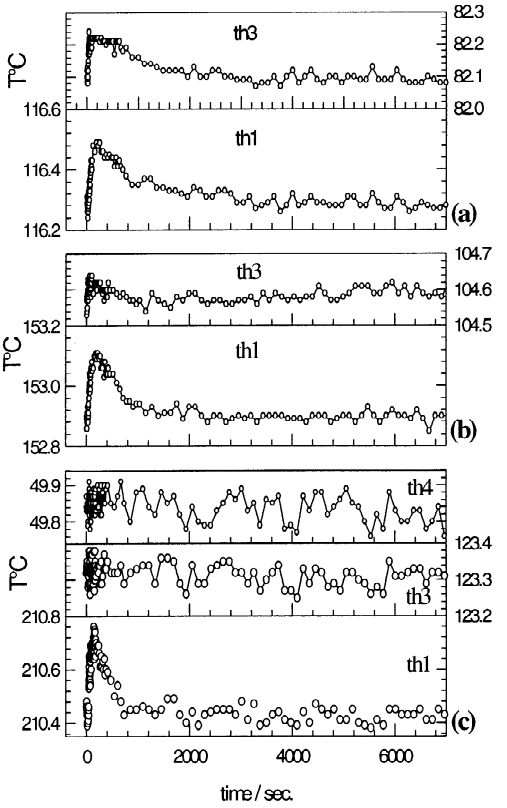

Fig. 4. Temperature variation inside the sample and above the thermopile, th1 = sample temperature, th3, th4 above thermopile; locations can be seen on Fig. 1.

peak 6), and at 210.6°C (Fig. 3c). The presence of the endothermal deviation is correlated with changes of the heat flow process as proven by the temperature variations (Fig. 4a) above the thermopile. Here, only part of the heat is detected. This state should correspond to the lower branch of the 'S' shaped curve. In that case, the calibration coefficient is overestimated leading to erroneously large heats of reaction. Approaching the upper limit of the transition, the absence of an endothermal contribution does not necessarily imply that redistribution of heat is not occurring, as for peaks 6 and 7 (Fig. 3b) with a plateau pressure of 1 kPa. Compared with Fig. 4a, the amplitude of the temperature variations in Fig. 4b are smaller but remain significant such that the endothermal effect is masked by the reaction. Finally at 210.6°C, according to the plateau pressure, $P = 20$ kPa, the gas is in a classical regime. The heat of reaction can be evaluated because the temperatures above the thermopile (Fig. 4c) are constant with typical fluctuations observed for convection in the gas phase. The results demonstrate that calorimetric measurements can be affected by artifacts which are identified by detecting the heat loss modifications within the reactor.

5. Modeling

We shall restrict ourselves to a brief account of the methodology and results, a complete analysis is given in Ref. [18].

5.1. Mono-dimensional case

5.1.1. Representation of the calorimeter cell

The cell arrangement is made of different concentric elements of known heat capacity and heat conductivity, in good or loose contact, where each interface represents an additional heat resistance. It is reduced to an equivalent system of three elements, as shown in Fig. 5 with (i) the heat source (HS), copper container and sample, (ii) the heat transfer domain reduced to a gaseous hydrogen film, the heat flux sensitive area being delimited by HS, (iii) the heat detector (HD) including the wall of the reactor and the thermopile.

5.1.2. Physical description

When the reactor is under vacuum the thermal resistance between the sample holder and the HD is large and the

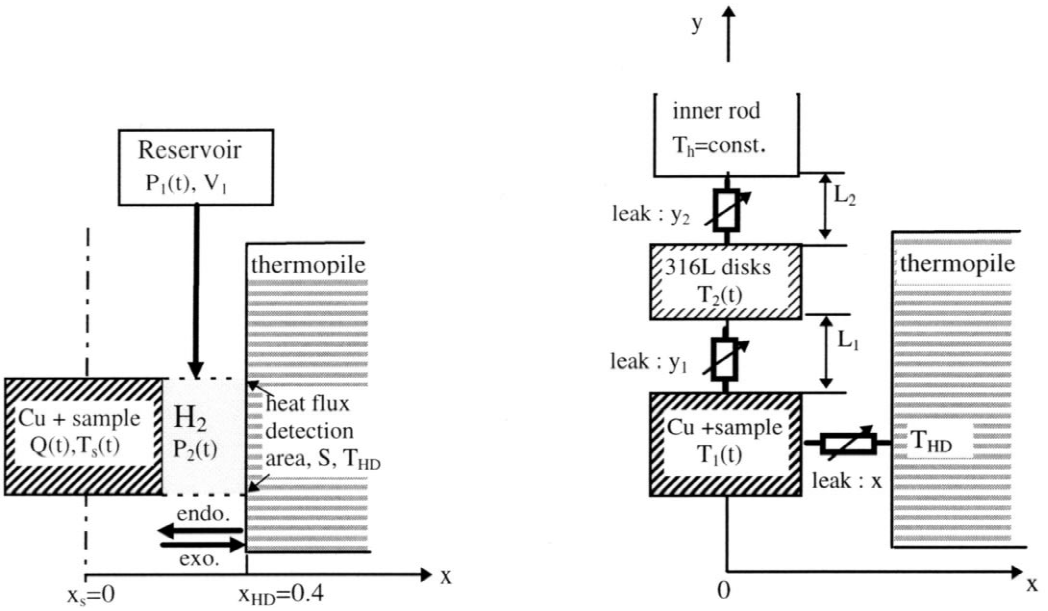

Fig. 5. Equivalent system representative of the calorimetric cell. Left, monodimensional case; right, bi-dimensional case.

sample temperature, T_s, is a few tenths of a degree lower than the temperature at the heat detector, T_{HD}. For this steady state, the baseline is shifted compared to the signal obtained with the true thermal equilibrium of the cell, e.g. $T_s = T_{HD}$. Thus, under vacuum, a small temperature gradient already exists between the sample and the HD. Unfortunately the temperature at the HD interface is not known exactly and will be given by the thermocouple in use for the temperature regulation of the furnace, T_r. Above the transition, the temperature readings indicate that $T_r = T_s = T_{HD}$.

This description is consistent with the assumptions: (i) at time $t = 0$, a temperature gradient exists between the heat source, $T_s(t)$, and the heat detector T_{HD}, the latter being constant, (ii) the temperature gradient is taken as linear due to the small thickness of the gaseous film, (iii) hydrogen mass transport for the transformation at the solid–gas interface is instantaneous all over the sample, meaning that $T_s(t)$ varies uniformly, (iv) the heat source is considered as punctual.

The thermal losses along the vertical axis being ignored, the cylindrical symmetry allows a simplification by solving the problem in one dimension. The calorimeter response, the pressures in the reference and reactor volumes, and the sample temperature are calculated and compared with the experimental data.

5.1.3. Equations of the model

The above assumptions lead to the heat balance equation:

$$\left(\frac{dQ}{dt}\right)^{\text{reaction}} + \left(\frac{dQ}{dt}\right)^{\text{leak}} = \left(\frac{dQ}{dt}\right)^{\text{capacity}}. \quad (1)$$

The first term is the heat source, part of which is dissipated through the gaseous film and part of which is accumulated, increasing the HS temperature. The resulting governing equation is:

$$|\Delta H| \times \frac{dn_H(t)}{dt} - \lambda_{H_2} \times S \times \frac{\delta T(t)}{\delta x} = mC \times \frac{dT_s(t)}{dt}. \quad (2)$$

ΔH is the relative enthalpy for the transformation, dn_H is the amount of hydrogen being absorbed, mC the contribution of the overall heat capacity of the sample and copper container. The linearity of the temperature gradient appears in the second term of Eq. (2) with:

$$\delta T = T_{HD} - T_s(t), \text{ and } \delta x = x_{HD} - x_s. \quad (3)$$

At the heat detector, the heat flux is given by:

$$\left(\frac{dQ}{dt}\right)^{HD} = \left(\frac{dQ}{dt}\right)^{\text{leak}}. \quad (4)$$

The mass balance for the reaction is:

$$\frac{dn_1}{dt} = \frac{dn_2}{dt} + \frac{dn_H}{dt} \quad (5)$$

where dn_1/dt corresponds to the mass of hydrogen transferred from the reference volume into the reactor, dn_2/dt, the number of moles accumulated in the reactor. The number of moles absorbed, dn_H/dt, satisfies the empirical rate equation [19] given by:

$$\begin{cases} \dfrac{dn_H}{dt} = \delta\left(\dfrac{H}{M}\right) \times n_M \times \dfrac{d\alpha}{dt} \\ \dfrac{d\alpha}{dt} = k_r\left[P_2(t) - P_{equ}(t)\right] \times (1-\alpha(t)) \times t^{N-1} \times N \end{cases} \quad (6)$$

with

$$\alpha(t) = \frac{\left.\dfrac{H}{M}\right|_t - \left.\dfrac{H}{M}\right|_{t=0}}{\left.\dfrac{H}{M}\right|_{t=\infty} - \left.\dfrac{H}{M}\right|_{t=0}},$$

$$\delta\left(\frac{H}{M}\right) = \left.\frac{H}{M}\right|_{t=\infty} - \left.\frac{H}{M}\right|_{t=0}. \quad (7)$$

dn_1/dt is calculated using the Poiseuille law and the ideal gas law:

$$\left.\frac{dP_1}{dt}\right|_t = \frac{k_v}{V_1}\left[P_1^2(t) - P_2^2(t)\right] \text{ and } P_1V_1 = n_1RT_1 \quad (8)$$

give:

$$\frac{dn_1}{dt} = \frac{V_1}{RT_1}\frac{dP_1}{dt} = \frac{k_v}{RT_1}\left[P_1^2(t) - P_2^2(t)\right] \quad (9)$$

where k_v is the characteristic of the needle valve, and P_1, P_2 are the pressure in the reference volume V_1 and the reactor V_2, respectively. Knowledge of dn_2/dt allows to calculate P_2 taking into account the temperature gradient in the reactor

$$\left.\frac{dP_2}{dt}\right|_t = R\left[\frac{1}{\sum_j\left[dV_j \times \dfrac{1}{T_{j+1}-T_j} \times \ln\dfrac{T_{j+1}}{T_j}\right]}\right] \times \frac{dn_2}{dt} \quad (10)$$

where T_j is the temperature affected to the element ΔV_j of the partitioned reactor volume [1].

5.1.4. Numerical applications

The set of differential equations is solved by a finite difference method with the appropriate boundary conditions.

Results of the global system simulation, *heat flux*, P_1, P_2, T_s are plotted in Fig. 6 (one representative experiment carried out at 116.3°C). The calculated pressures, Fig. 6a–a′, reproduce quite accurately the experimental variations, justifying the choice of the rate equation. Comparison between the shape of the simulated and experimental thermograms, Fig. 6b, shows that a very good agreement is obtained up to 400 s, duplicating the shape of the endothermal effect. Using the calibration constant, k_c, the measured heat of transformation gives $\Delta H = -61$ kJ/mol H, much more exothermic than the true value, $\Delta H = -34$ kJ/mol H [15,16]. At that point, the model does not prove that k_c is not valid for the dynamic conditions of hydrogen transfer, but it confirms that the parameters used in λ_{H_2} governing heat transfer through the gas phase are satisfactory. Finally the calculated sample temperature T_s and the measured Th_1 are reported in Fig. 6c indicating the presence of a marked discrepancy between them. The calculated temperature is too high, ~0.16°C at the maximum. This suggests that the heat of transformation used for the calculation is too large and justifies the fact that, now, k_c is no longer valid for the experimental conditions.

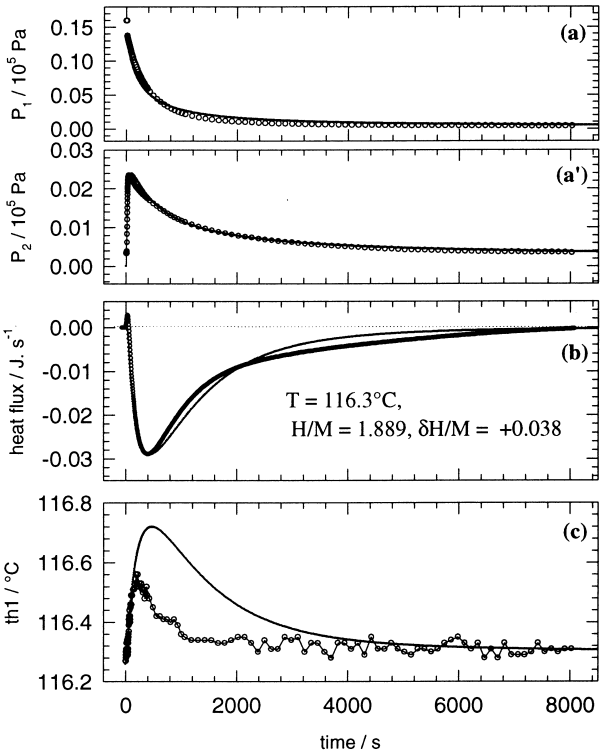

Fig. 6. Comparison measurements (symbols)/model (lines): (a) pressure in V_{ref}, (a′) pressure in reactor, (b) thermogram, (c) sample temperature.

In the low pressure range, assuming a temperature gradient between the heat detector and the sample container, the model generates an endothermal effect. Simultaneously the shape of the signal detected is weighted by the heat transfer in the gas phase and thus by the thermal conductivity of the hydrogen gas. A temperature gradient makes the simple model relatively correct for this purpose. However, when the pressure slowly increases the temperature gradient diminishes as well as the endothermal contribution and the model is no longer appropriate to simulate all the different experimental quantities, *heat flux*, P_1, P_2, T_s.

5.2. Bi-dimensional case

5.2.1. Physical description and equations

To take into account the heat loss in the *Y* direction, the equivalent system is modified as shown in Fig. 5. In the new configuration, the first heat leak occurs between the sample container at $T_1(t)$ and the equivalent representation of the stainless steel fins at $T_2(t)$. The second contribution

is concerned by the leak between the fins and the inner rod at temperature T_h = const. Along the vertical path, heat transfers between the elements through the guides which are used to support the container and the fins. The modifications require new expressions of the thermal balance, which has to be evaluated at the sample container,

$$\left(\frac{dQ}{dt}\right)^{reaction} + \left(\frac{dQ}{dt}\right)^{leak,x} + \left(\frac{dQ}{dt}\right)^{leak,y1} = \left(\frac{dQ}{dt}\right)^{capacity} \quad (11)$$

and at the fins level,

$$\left(\frac{dQ}{dt}\right)^{leak,y1} + \left(\frac{dQ}{dt}\right)^{leak,y2} = \left(\frac{dQ}{dt}\right)^{capacity} = m_2 \times Cp_2 \times \frac{dT_2(t)}{dt} \quad (12)$$

with:

$$\left(\frac{dQ}{dt}\right)^{leak,y1} = \lambda_{ss} \times S_1 \times \frac{[T_1(t) - T_2(t)] - [T_1^0 - T_2^0]}{L_1} \quad (13)$$

and

$$\left(\frac{dQ}{dt}\right)^{leak,y2} = \lambda_{ss} \times S_2 \times \frac{[T_2(t) - T_h(t)] - [T_2^0 - T_h]}{L_2}. \quad (14)$$

Eqs. (13) and (14) indicate that the vertical leak is induced by the difference between the temperature gradient taken at time t and the corresponding value in the steady state, e.g.:

$$T_1(t=0) = T_1(t=\infty) = T_1^0 \text{ and } T_2(t=0) = T_2(t=\infty) = T_2^0.$$

5.2.2. Numerical applications

The calculations have been made for one representative experiment at 152.9°C (within the Knudsen domain) Fig. 7, and at 226.2°C (above the domain) Fig. 8.

The overall rate law is obviously not affected by taking into consideration the heat leak through the vertical axis. It turns out that the calculated pressures keep their agreement with the experimental values, Fig. 7a–a′ and Fig. 8a–a′. Now, the model is able to reproduce the thermograms in excellent agreement with the experimental ones, Figs. 7b and 8b. It must be pointed out that at 152.9°C, despite the fact that the system is in the Knudsen region, the endothermal contribution is quickly overcome by the heat of transformation and the model follows that behavior.

The final test on the validity of the model is provided by the calculated temperatures within the sample and above the thermopile. Although the temperature variations remain small (of the order of 0.3°C and 0.15°C for the sample and the thermocouple located above the thermopile, respectively), the calculated and measured maximum temperature increases of the sample give now the same value, Fig. 7c. However, when the sample temperature decreases, a slight discrepancy is maintained, 0.06°C. This behavior is also

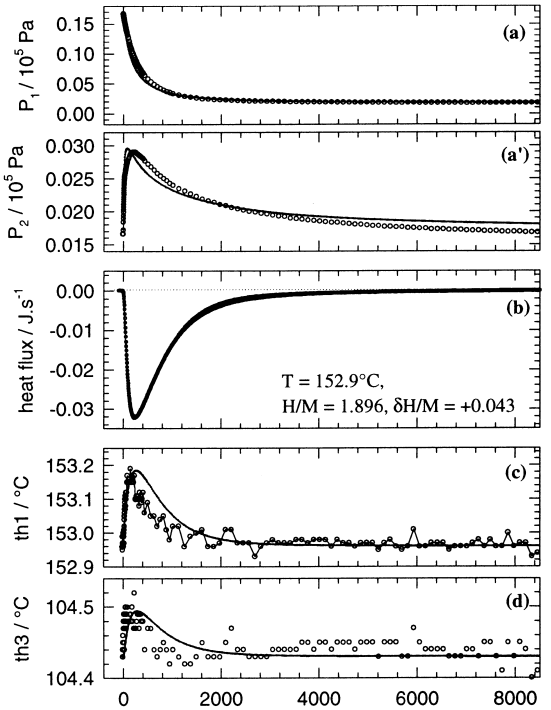

Fig. 7. T = 152.9°C, comparison measurements (symbols)/model (lines): (a) pressure in V_{ref}, (a′) pressure in reactor, (b) thermogram, (c) th1 = sample temperature, (d) th3 = temperature above thermopile.

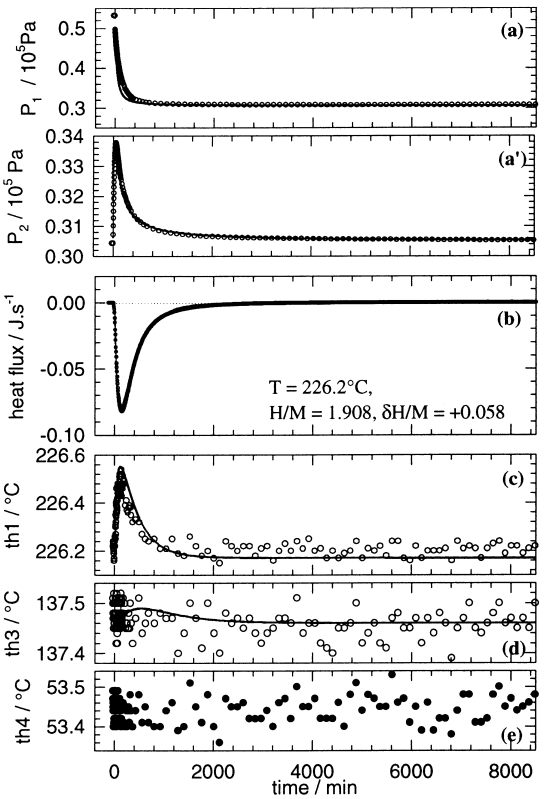

Fig. 8. T = 226.2°C, comparison measurements (symbols)/model (lines): (a) pressure in V_{ref}, (a′) pressure in reactor, (b) thermogram, (c) th1 = sample temperature, (d, e) th3, th4 = temperatures above thermopile.

reproduced for the thermocouple located above the thermopile, Fig. 7d. At 226.2°C the agreement between calculated and measured temperatures is even better, demonstrating that the model is sensitive enough to simulate all the parameters of the system and is able to take into account the modification of the heat losses above the thermopile.

6. Conclusions

In this research we have analyzed the validity of the enthalpies determination for the reaction of H_2(g) with ZrNi. Experimentally and confirmed by modeling of the calorimeter cell, it has been shown that below (or close) to the Knudsen transition, the heat measurements are invalid and could lead to misinterpretation of the data. This problem is a very general one, which can be observed in any other solid/gas system in the low pressure range such as metal oxide/oxygen(g), and is also relevant in heat of adsorption measurements in porous systems. In this work, heat measurements become meaningful at 210°C. The average values of the relative enthalpies for $\beta \rightarrow \gamma$ transformation, trihydride formation, and $\gamma \rightarrow \beta$, trihydride decomposition are $\Delta H^{f} = -34.3 \pm 0.5$ kJ/mol H and $\Delta H^{d} = 34.4 \pm 0.5$ kJ/mol H. A detailed analysis of the thermodynamic properties of the system is given elsewhere [16].

Acknowledgements

The authors thank Pr. T.B. Flanagan (University of Vermont, USA) for criticisms and judicious discussion and R.C. Bowman Jr. (JPL, CA, USA) for providing us with a sample of closely stoichiometric ZrNi of high purity.

References

[1] P. Dantzer, P. Millet, Rev. Sci. Instrum. 71 (2000) 142.
[2] S.L. Randzio, J.P. Grolier, J.R. Quint, Rev. Sci. Instrum. 65 (1994) 960.
[3] V. Torra, H. Tachoire, Thermochim. Acta 203 (1992) 419.
[4] J.F. Fernandez, F. Cuevas, C. Sanchez, J. Alloys Comp. 298 (2000) 244.
[5] V. Torra, H. Tachoire, J. Therm. Anal. 52 (1998) 663.
[6] W. Hemminger, G. Höhne, Calorimetry — Fundamentals and Practice, Verlag Chemie, Berlin, 1984.
[7] W. Zhang, M.P.S. Kumar, A. Visintin, S. Srinivasan, H.J. Ploehn, J. Alloys Comp. 242 (1996) 143.
[8] K. Watanabe, K. Tanaka, M. Matsuyama, K. Hasegawa, Fusion Eng. Design 18 (1991) 27.
[9] N. Mitsuishi, S. Fukada, N. Tanimura, J. Less Common Metals 123 (1986) 65.
[10] R.C. Bowman, P.B. Karlmann, S. Bard, Brilliant Eyes Ten-Kelvin Sorption Cryocooler Experiment (BETSCE), Final Report, 1997, JPL Publication 97-14.
[11] G.G. Libowitz, H.F. Hayes, T.R.P. Gibb, J. Phys. Chem. 62 (1958) 76–79.
[12] M.E. Kost, L.N. Padurets, A.A. Chertkov, V.I. Mikheeva, Russ. J. Inorg. Chem. 25 (1980) 471, translated from Zhurnal Neorganicheskoi Khimii, 25 (1980) 847.
[13] D.G. Westlake, H. Shaked, P.R. Mason, B.R. McCart, M.H. Mueller, J. Less-Common Metals 88 (1982) 17.
[14] M. Gupta, J. Alloys Comp. 293–295 (1999) 190.
[15] W. Luo, A. Craft, T. Kuji, H.S. Chung, T.B. Flanagan, J. Less Common Metals 162 (1990) 251.
[16] P. Dantzer, P. Millet, T.B. Flanagan, Metall. Mater. Trans 32A (2001) 29.
[17] E.H. Kennard, Kinetic Theory of Gases, McGraw Hill, New York, 1938.
[18] P. Dantzer, P. Millet, Thermochim. Acta 370 (2001) 1.
[19] H.Y. Cai, P. Millet, P. Dantzer, J. Alloys Comp. 231 (1995) 427.